Observations on the non-mixed length and unsteady shock motion in a two dimensional supersonic ejector

Article *in* Physics of Fluids · February 2014

DOI: 10.1063/1.4868879

CITATIONS
66

READS
1,875

2 authors:

Srisha M.V. Rao
Indian Institute of Science
76 PUBLICATIONS **448** CITATIONS

SEE PROFILE

Jagadeesh Gopalan
Indian Institute of Science
297 PUBLICATIONS **2,376** CITATIONS

SEE PROFILE

Observations on the non-mixed length and unsteady shock motion in a two dimensional supersonic ejector

Srisha M. V. Rao and Gopalan Jagadeesh

Citation: Physics of Fluids (1994-present) **26**, 036103 (2014); doi: 10.1063/1.4868879
View online: http://dx.doi.org/10.1063/1.4868879
View Table of Contents: http://scitation.aip.org/content/aip/journal/pof2/26/3?ver=pdfcov
Published by the AIP Publishing

PHYSICS OF FLUIDS **26**, 036103 (2014)

Observations on the non-mixed length and unsteady shock motion in a two dimensional supersonic ejector

Srisha M. V. Rao[a] and Gopalan Jagadeesh[b]
Department of Aerospace Engineering, Indian Institute of Science, Bengaluru - 560012, India

(Received 26 September 2013; accepted 6 March 2014; published online 21 March 2014)

Key features that drive the operation of a supersonic ejector are the complex gasdynamic interactions of the primary and secondary flows within a variable area duct and the phenomenon of compressible turbulent mixing between them, which have to be understood at a fundamental level. An experimental study has been carried out on the mixing characteristics of a two dimensional supersonic ejector with a supersonic primary flow (air) of Mach number 2.48 and the secondary flow (subsonic) which is induced from the ambient. The non-mixed length, which is the length within the ejector for which the primary and secondary flow remain visually distinct is used to characterize the mixing in the ejector. The operating pressures, flow rates and wall static pressures along the ejector have been measured. Two flow visualization tools have been implemented—time resolved schlieren and laser scattering flow visualization. An important contribution has been the development of in-house image processing algorithms on the MATLAB platform to detect the non-mixed length from the schlieren and laser scattering images. The ratio of mass flow rates of the secondary flow to primary flow (entrainment ratio) has been varied in a range of 0.15–0.69 for two locations of the primary nozzle in the ejector duct. Representative cases have been computed using commercial CFD tool (Fluent) to supplement the experiments. Significant outcomes of the study are—the non-mixed length quantified from the flow visualization images is observed to lie within 4.5 to 5.2 times the height of the mixing duct which is confirmed by the wall static pressure profiles. The flow through the supersonic ejector in the mixed regime is explained using corroborative evidences from different diagnostic tools. A reduction of the non-mixed length by 46.7% is observed at operating conditions when the nozzle is sufficiently overexpanded. The disturbance caused to the mixing layer due to unsteady shock-boundary layer interactions within the nozzle at such conditions enhances mixing. The analysis of time resolved schlieren images have provided interesting observations on repetitive back and forth motion of the shock cells in the primary flow with a co-flowing secondary flow in the confines of the supersonic ejector. The oscillations have significant amplitudes (order of the nozzle height) at the centerline. The details of these experiments followed by the analysis of data and the inferences drawn from the results are discussed in this article. [http://dx.doi.org/10.1063/1.4868879]

I. INTRODUCTION

A supersonic ejector is a gasdynamic device that uses a supersonic primary flow to pump a co-flowing secondary flow by means of momentum and energy augmentation in a variable area duct. With simplicity in construction and operation being its greatest advantage, ejectors have found applications in thrust augmentation,[1–3] jet noise reduction, starting load reduction in aerodynamic test facilities,[4–6] refrigeration technology,[7,8] gasdynamic lasers,[9] recirculation of fuel in fuel cells,[10]

[a]Electronic mail: srisharao@aero.iisc.ernet.in
[b]Electronic mail: jaggie@aero.iisc.ernet.in

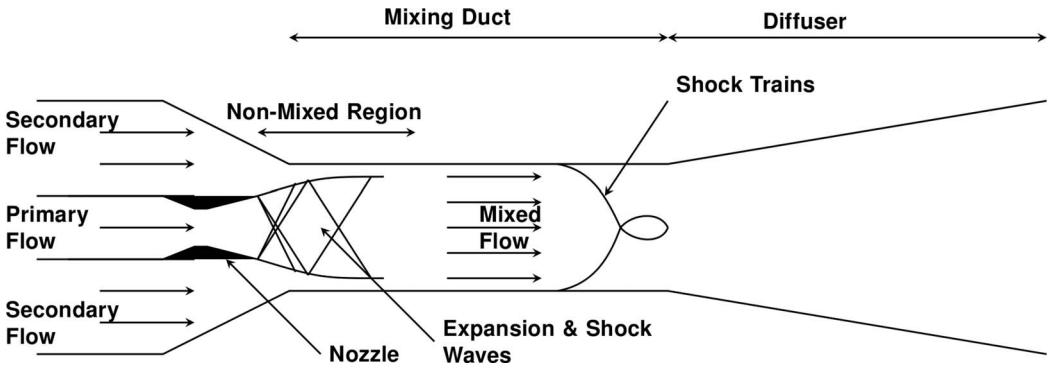

FIG. 1. Diagrammatic representation of the flow features in a supersonic ejector.

a device to dilute and purge gases, to list a few. Figure 1 is a schematic of a typical supersonic ejector, showing the different physical components as well as typical flow features that are experienced by the flow in an ejector. The secondary flow is induced into the mixing duct by suction and entrainment generated by the supersonic primary flow. A compressible turbulent mixing layer separates the two streams initially, through which momentum and energy are exchanged between them. The two flows eventually mix in the mixing duct, and the mixed flow may experience shocks before its velocity is brought to subsonic values. A divergent subsonic diffuser ensures the final pressure recovery.

The functioning and performance of the ejector is solely dictated by the complex gasdynamic flow occurring within it consisting of shocks, shear layers, and their interactions. Previous experimental studies had focused on mapping the performance characteristics of the ejector which is useful in validation of design methodologies for the ejector.[11,12,14–16] A significant observation was the phenomenon of the secondary flow choking[14] which limited the maximum flow rate through the ejector, and this choked regime was investigated extensively. The mixed regime of supersonic ejector operation involves a subsonic secondary flow that does not choke, hence providing a channel for upstream communication of pressure and thereby making the operation of the ejector highly sensitive to the backpressure. Generally, ejectors function in the mixed regime of operation. They are operated in the choked regimes only for particular applications where choking can be advantageous, for example, in refrigeration applications.[8] Even when designed for choked operation, the off-design operation is in the mixed regime. Details of flow phenomena in this regime are unexplored.

Control volume methods were used to devise relations among non-dimensional performance parameters—the entrainment ratio, the stagnation pressure ratio (ratio of stagnation pressures of the primary and secondary flow), the compression ratio (ratio of the exit pressure to the secondary stagnation pressure). The geometry of the ejector passage was taken into account by the Mach number of the primary flow and ratio of the area of the mixing duct to the nozzle exit area known as the area ratio.[11,12] A key design variable that is unknown when sizing the ejector by control volume methods is the length of the mixing duct which is dependent on the mixing characteristics of the flow. In practice, *ad hoc* mixing duct lengths have been used determined from rule of thumb guidelines without firm empirical or theoretical support. Determining the mixing characteristics of the ejector is of importance for consistent and improved design.

Reduction in the rate of mixing at high Mach number (more specifically high convective Mach number) was observed in studies on canonical compressible mixing layer[20,21] or open jet geometries where the static pressure imposed upon the mixing layer is maintained more or less constant. The confinement of the supersonic jet and the co-flowing secondary flow between the walls of the ejector passage significantly alters the flow topology in comparison to such geometries. Unlike open domain flows, the mixing layer is subjected to pressure gradients imposed by the acceleration of the secondary flow and the geometry of the variable area duct. The shock cell structure within the jet core also responds to these factors. The interplay of flow and aeroacoustic characteristics are also altered in a confined duct.

Much of the previous experiments on the ejector had been conducted in tubular opaque geometries which limit the use of flow visualizations tools. A few qualitative schlieren visualizations

aimed at a flow scenario when both primary and secondary flows are supersonic and a study of the ensuing shock structures were conducted.[17,18] Qualitative visualization of the flow in an ejector by scattering of light from a laser sheet by particles seeded in either of the two flows was carried out in a cylindrical ejector[13] and the non-mixed length defined as the length within the ejector for which the primary and secondary flow remain visually distinct, was qualitatively identified in the images. The distortion of the field of view due to the curvature of the transparent cylindrical walls makes quantitative analysis cumbersome.

The lacuna in a comprehensive understanding of the flow physics through a supersonic ejector in general, especially the mixing characteristics and operation in the mixed regime in particular motivated the authors towards a study on supersonic ejectors using theoretical, experimental, and numerical methods. The focus of the present study is to understand the gasdynamics and mixing process within a two dimensional supersonic ejector in the mixed regime using quantitative optical diagnostic tools and wall static pressure measurements. A high aspect ratio rectangular cross section ejector is used so that quantitative flow visualizations can be effectively carried out. The control volume technique is used with a bio-inspired optimization technique to arrive at an optimized ejector geometry.[22] Two flow visualization techniques are implemented—time resolved schlieren and laser scattering from acetone particles seeded in the primary flow. In this work, the authors characterize mixing in terms of the non-mixed length. The non-mixed length can be considered as a visual mixing length that can be identified from flow images and is directly proportional to the length of mixing in the ejector. Trends derived from observations on the non-mixed length should have a direct bearing on the actual length of mixing in the ejector. Image processing algorithms are developed to quantitatively determine the non-mixed length in the ejector from the flow images. Exhaustive experiments are carried out for two locations of the primary nozzle within the ejector mixing duct and for a range of entrainment ratios (0.12–0.69) achieved by varying the secondary flow rate and the primary stagnation pressure. RANS equations on a two dimensional grid are solved for representative cases using Fluent to supplement the experimental observations. Details of the experimental setup, a brief description of the flow visualization techniques and the image processing methodology, followed by an elaboration of the results at salient experimental conditions that clearly bring out the physics of the flow through a supersonic ejector are discussed in this article. Supportive evidences from numerical computations are also given. While much of the article deals with statistically steady description of the flow, the unsteady nature that can be observed in time resolved schlieren images are discussed at the end, followed by conclusions of this study.

II. EXPERIMENTAL FACILITY

A supersonic ejector test rig is established at the Laboratory for Hypersonic and Shockwave Research, Indian Institute of Science, which is described in brief here and the details are provided in the doctoral thesis.[23] The requirements of flow diagnostics, sufficient flexibility for variation of operating parameters as well as limitations imposed by a laboratory scale study are considered while designing the setup. Figure 2 shows diagrammatically the two dimensional supersonic ejector test rig. The constant area of the mixing duct is 20 mm in height, 80 mm in width, and 200 mm in length which is preceded by a convergent passage converging from 60 mm height in a length of 60 mm. The diffuser section is 200 mm in length and diverges to a height of 60 mm. The primary supersonic nozzle has an exit height of 6 mm and a throat of 2.3 mm giving a designed Mach number of 2.48. The supersonic nozzle side walls butt the side walls of the ejector such that room for flow at the corners of the rectangular geometry is negligible. The rectangular geometry presents a higher shear perimeter to the mixing layer than a circular cross section nozzle and the flow at the corners of the rectangular nozzle may significantly affect the mixing dynamics. It was observed that the difference in mixing rate between cylindrical and non-cylindrical nozzle geometries due to perimeter stretching was generally small even at large aspect ratios.[19] Thus similarity in trends is to be expected between more practical tubular geometries to what has been observed in the rectangular geometry and the utility of the observations towards design is appreciable.

The primary flow is supplied from compressed air reservoirs of capacity 6 cubic meters at a maximum pressure of 12.5 bars via a stagnation chamber, where the stagnation pressure of the

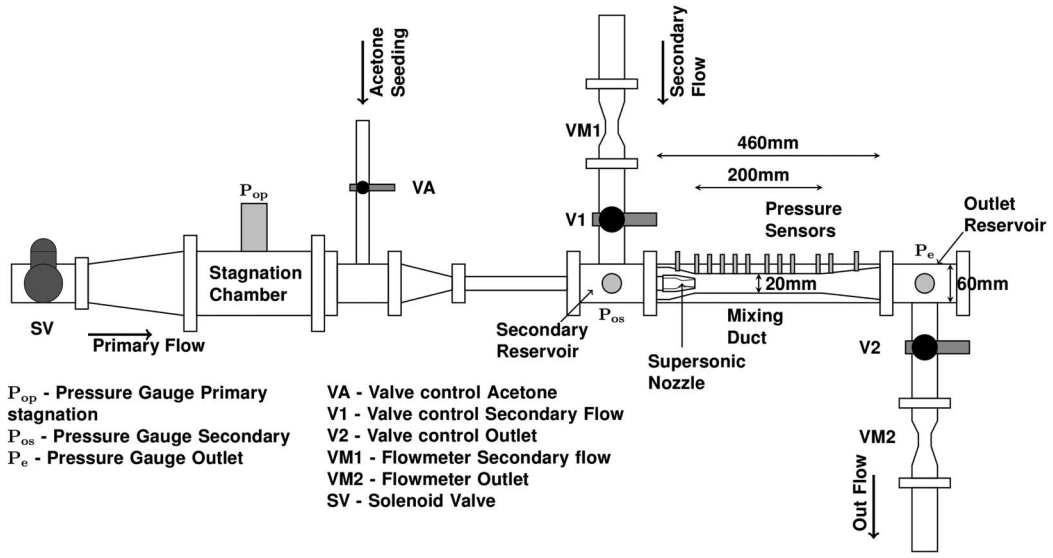

FIG. 2. Schematic of the two dimensional supersonic ejector setup.

primary flow is measured. The stagnation pressure of the primary flow is controlled by a pressure regulator and the blow down operation is executed by a solenoid valve. The secondary flow enters the ejector via straight section of pipe which then takes a right angle bend to an intermediate secondary reservoir before entering the ejector section. Similarly, the outflow proceeds from the diffuser to an outlet reservoir from where the flow turns to a straight pipe that opens to the ambient. Venturimeter (VM1) measures the secondary flow rate which is controlled by a valve (V1). The outlet flow rate is measured using venturimeter (VM2) and the primary flow rate is deduced by the difference of secondary flow rate from the outlet flow rate. The operating pressures of the secondary flow and the outlet flow are measured at the reservoir stations (P_{os} & P_e, respectively). The side walls and the end flange at the outlet reservoir have transparent optically polished BK-7 glass (19 mm thick) windows for flow visualization. 12 Kulite pressure transducers (XCS-062) are mounted on the top wall of the ejector to measure the wall static pressure profile along the ejector. The sensors are closely spaced along the mixing duct while presence of flanges and fasteners hinders the spacing at other locations. A Dewetron (24 bit resolution, 16 channels) data acquisition system is used to record the signals from the transducers at 20 kHz and is triggered automatically upon the start of the ejector. Note that the flow through the ejector is from left to right, and that the X = 0 of the plot corresponds to the beginning of the two dimensional ejector setup further upstream of the nozzle exit location. Two flow visualization techniques are implemented to capture the details of the flow structure within the ejector which are described in brief here.

A. Time resolved schlieren

A standard Z-type schlieren arrangement[25] is used as shown diagrammatically in Figure 3. A halogen light source of 250 W is used with a condenser lens system to achieve a point source of high intensity light. The knife edge is placed vertically at the focus. A Phantom V310 high speed camera is used at a pixel resolution of 1280 × 800 and at a frame rate of 2000 fps to capture the time resolved schlieren images. The imaging window begins upstream of the nozzle exit, captures the whole of the constant area section and ends just at the start of the diffuser. Good quality of schlieren images where in fine details of the flow structure are captured sharply is important for image processing which is based on the identification of these structures of the flow. The parameters for schlieren visualizations of such crispness is arrived at after a series of experiments using different light sources and exposure settings which gave different contrasts and smearing of the gradients due to averaging effects.[23] Finally, the image captured at 6 μs exposure time with a high intensity light

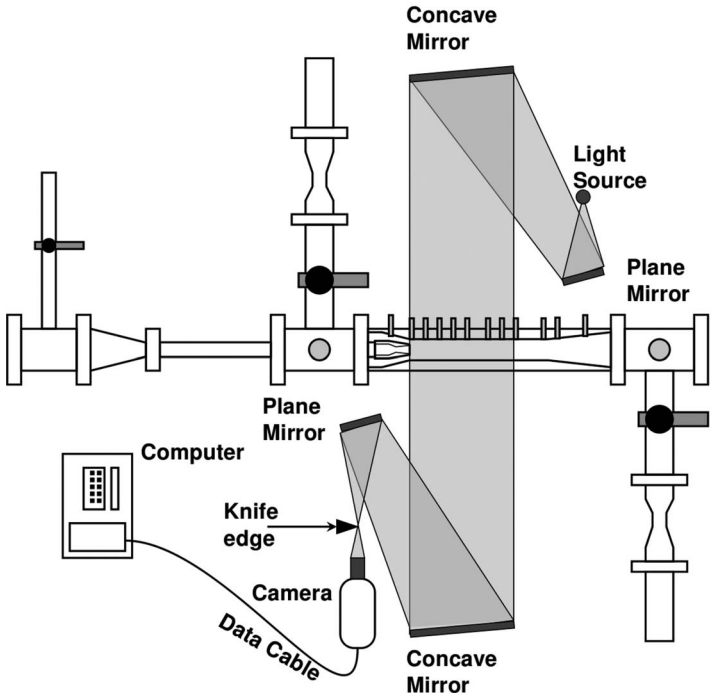

FIG. 3. Schematic of the Z-type arrangement for schlieren visualizations of the flow through the ejector.

source showed the best possible contrast and sharpness of the structures within the limits of camera and the light source.

B. Laser scattering flow visualization technique

The schlieren reveals density gradients within the flow. However, since neither the primary flow nor the secondary flow are marked, the progress of mixing within the ejector duct is inferred from the flow structures. To obtain clear indications on mixing characteristics, the primary flow is seeded with acetone vapors which condense to form fine particles on expansion through the nozzle thus seeding the flow with Mie scattering tracers. Essentially borrowed from the vapor screen method,[27] the method has been suitably applied to the current application. A similar technique using ethanol vapors was extensively used to study a canonical compressible mixing layer and the details of the technique was described by Clemens and Mungal.[21,28] The "passive scalar" method of Mie scattering visualization is used here. The acetone mass fractions are kept small (about 0.0005–0.0008) so that negligible changes are introduced into the flow in the ejector due to seeding. The wall static static pressure in the ejector when seeded with acetone tracers varies from the unseeded flow within $1\% \approx 2\%$ at different experimental conditions, implying minimal changes to the flow field due to seeding. A laser sheet is passed through the mid-section of the ejector width from the transparent end flange at the outlet reservoir as shown in the schematic in Figure 4. The 532 nm wavelength of a Nd-YAG laser (Spectra Physics Quantaray LAB-170, at 180 mJ energy and 10 Hz pulse rate) is taken with suitable sheet optics that renders the beam to a very thin sheet, which is passed into the ejector. The same Phantom camera is used to record the laser scattering images.

C. A note on experimental uncertainties

The experiments have been conducted carefully and repeated for statistical consistency and reliability. However, given the accuracy of instrumentation, behavior of mechanical flow control elements, limitations of the digital data acquisition, uncertainty in the reported values is unavoidable

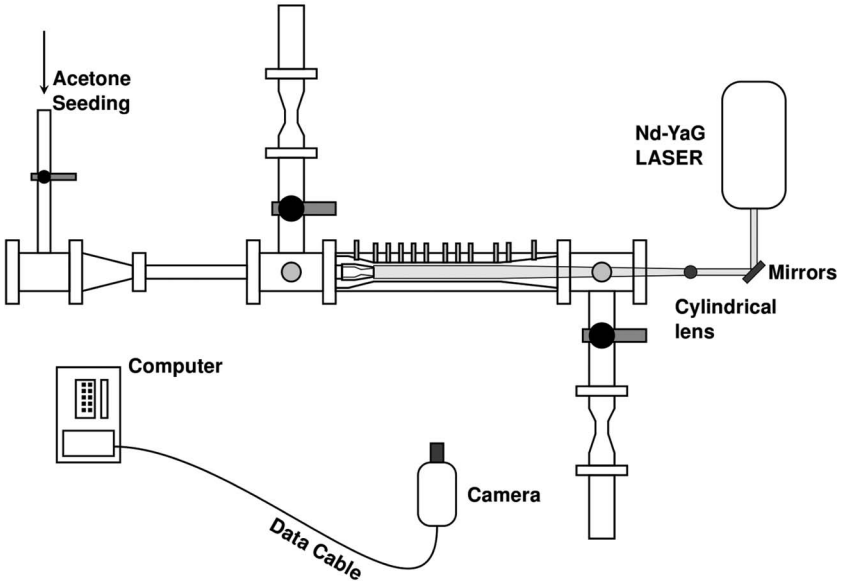

FIG. 4. Schematic of the arrangement for laser scattering flow visualizations.

which can propagate to the derived parameters. The flow rates are measured to ±5% uncertainty. The primary flow stagnation pressure can be maintained to ±2% and taking the instrumentation of pressure sensors into account an uncertainty of ±4% is expected in the pressure measurements.

III. NUMERICAL COMPUTATIONS

While experimentation has been the dominant methodology to study the flow through a supersonic ejector in the mixed regime, numerical simulations are carried out using commercial CFD package Fluent for representative cases to supplement the experimental observations. The steady compressible RANS equations are solved on a two dimensional grid for half the geometry of the ejector taking the centerline as a symmetry plane. A fine grid of 0.5×10^6 cells is used with appropriate refinement of the grid at regions of high gradients in the flow.[23] Following the recommendations of Bartosiewicz *et al.*,[29] the k-ω SST turbulence model is used to model turbulence. The stagnation pressure of the primary flow, the secondary flow mass flow rate, and the outlet backpressure are the boundary conditions used. The computations are carried out such that first, the residuals converge and second, the mass balance is ensured across the boundaries for which the boundary pressures are adjusted. Often, this results in the boundary pressure being different from the experimental value.

IV. EXPERIMENTAL CONDITIONS AND ANALYSIS OF DATA

Exhaustive experiments have been conducted in the mixed regime of ejector operation. The nozzle is placed at two locations within the mixing duct, one just at the entrance of the constant area section of the mixing duct (Location A, 160 mm) and the second at 15 mm upstream of the constant area section inside the convergent passage (Location B, 145 mm). Corresponding to each location of the nozzle the primary stagnation pressure (P_{op}) is varied (5.69, 7.69, and 9.69 bars absolute) and the secondary flow rate is varied by adjusting the valve V1 (resulting in entrainment ratios 0.12–0.69). Detailed discussions of the results given in this article pertains to the maximum entrainment ratio at each primary stagnation pressure as tabulated in Table I.

A. Wall static pressure measurements

A typical raw pressure signal obtained during a run of the ejector is shown in Figure 5. The starting and stopping of the primary flow during the blow down operation is reflected in the initial

TABLE I. Table of experimental conditions.

Sl. no.	Nozzle position	Primary stagnation pressure P_{op}	Secondary stagnation pressure P_{os}	Exit pressure P_e	Primary mass flow rate $\dot{m}_p$	Secondary mass flow rate $\dot{m}_s$	Stagnation pressure ratio $\frac{P_{op}}{P_{os}}$	Compression ratio $\frac{P_e}{P_{os}}$	Entrainment ratio $\frac{\dot{m}_s}{\dot{m}_p}$
1	Location A	9.69	0.86	1.51	0.434	0.093	11.29	1.76	0.21
2		7.69	0.86	1.29	0.335	0.116	8.96	1.50	0.34
3		5.69	0.87	1.17	0.236	0.135	6.56	1.34	0.57
4	Location B	9.69	0.86	1.53	0.434	0.103	11.22	1.77	0.24
5		7.69	0.86	1.34	0.335	0.148	8.92	1.56	0.44
6		5.69	0.86	1.14	0.236	0.163	6.61	1.33	0.69

drop and the final rise of the signal, while the signal remains steady for a good duration (about $2 \approx 3$ s) in between the opening and closing of the valve. A one second segment of the signal away from the starting and stopping transients is taken as the test time for analysis. The signal is filtered, averaged over time, and then divided by the sensitivity of the sensor to obtain the pressures in physical units. A statistically steady mean pressure is obtained from each sensor with a deviation of $<2\%$ over the mean during the test time and the pressure values reported here are an ensemble average of the mean pressure for five runs at the same experimental condition. The pressure measurements have been found to be repeatable and the deviation from the ensemble average is within the experimental uncertainty for all the cases reported here.

B. Digital image analysis for detection of non-mixed length

Complete details of the processing of images using in-house codes can be found in Refs. 23 and 24, which is described briefly here by taking a template case as an example.

1. Image processing of schlieren images

Fine details of the flow including transient turbulent structures are frozen in the schlieren image as seen in a typical instantaneous schlieren image of the flow through the ejector at a primary stagnation pressure of 7.69 bars, Figure 6.

The shock cells, mixing layer, and structures spanning the height of the duct can be clearly seen in the figure. The non-mixed region, the region within the duct where the two flows are distinct, can be visually observed and is marked on the image. At the end of the non-mixed region the flow enters a region of increased mixing with large scale turbulent structures spanning the height of the duct

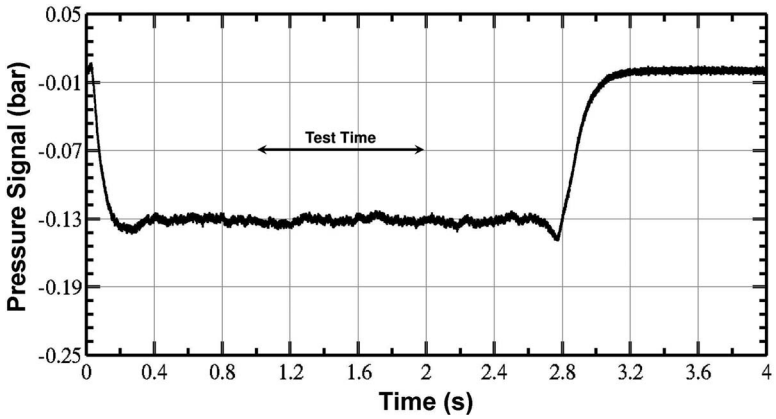

FIG. 5. A typical pressure signal during the experiment, $P_{op} = 9.69$ bars, nozzle exit at Location A, 160 mm.

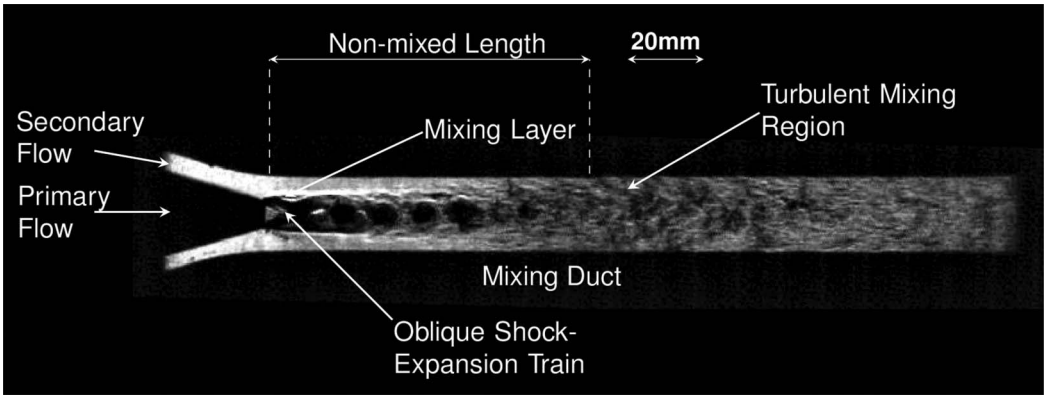

FIG. 6. An instantaneous schlieren image of the flow through the supersonic ejector at $P_{op} = 7.69$ bars, nozzle exit at Location A, 160 mm.

termed as the turbulent mixing region. The fact that by the end of the non-mixed region the flow is dominated by turbulent structures is exploited to quantitatively determine the non-mixed length by image processing algorithms developed at the laboratory using MATLAB functions. Absence of shock structures at the end of the constant area duct indicates the presence of subsonic flow.

Pre-processing of the images involve contrast adjustment and cropping to the area of analysis. The area of interest extends from the exit of the nozzle to the end of constant area section. X refers to the streamwise direction along the ejector and Y the transverse direction along the height of the mixing duct. The scale of the image is determined by extracting the number of pixels corresponding to a reference length—the height of the mixing duct (20 mm), from the image. The spatial resolution of the image is about 3 pixels/mm. Thereafter, the image is passed through Canny edge enhancement subroutine[26] that emphasizes sharp edges corresponding to shocks, mixing layer, and turbulent structures (the walls are excluded from analysis). The edge enhanced figure of the image in Figure 6 is shown in Figure 7. Besides the walls; shock cells, mixing layer edge, and random structures in the turbulent mixing region are highlighted. Notice that the density of edges increases in the midst of the turbulent mixing region.

The variation of intensity of the edge enhanced image in Figure 7 across vertical lines along the ejector is given in Figure 8. Each peak corresponds to the location of an edge in the edge enhanced image. At distance of 5 mm–40 mm from the nozzle exit the dominant edges are due to the shock cell or the mixing layer, where the primary flow and secondary flow can be separately identified. From about 80 mm–100 mm the density of edges have increased greatly since this region now lies in the turbulent mixing zone. These edges correspond to the turbulent structures that span the entire duct height. Thus the non-mixed length must lie about this value which is identified algorithmically by defining a suitable mixing parameter that can capture this behavior. The ratio of the average intensity to the maximum intensity of the edge enhanced image along a vertical line in the flow section is defined as the mixing parameter β_{mix} which is given in Eq. (1), where I is the intensity at a pixel and H is the height of the mixing duct. In the non-mixed region where the number density of edges is less, (only the edges corresponding to shock and mixing layer are detected) the magnitude of β_{mix} is low. β_{mix} starts increasing with the thickening of the mixing layer within which structures get detected.

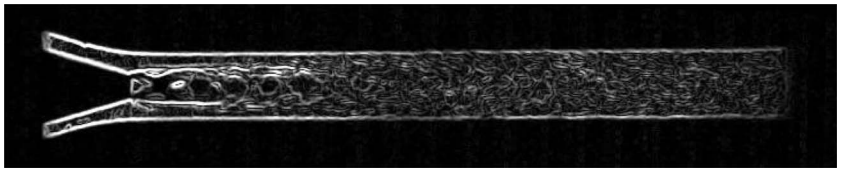

FIG. 7. The edge enhanced image corresponding to the image in Figure 6.

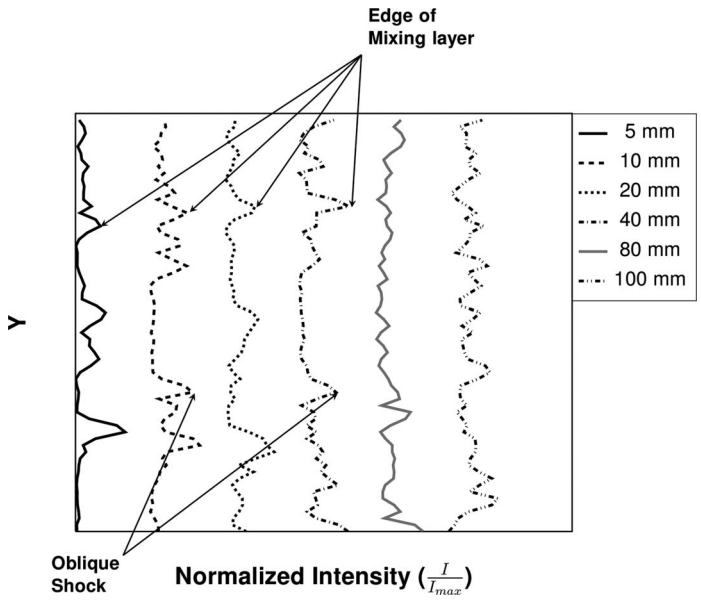

FIG. 8. Intensity variation across the height of the mixing duct in the edge enhanced image, Figure 7, at various downstream locations from the nozzle exit, nozzle exit at 160 mm.

Maximum values, close to unity, occur after the end of the potential core of the supersonic jet in the turbulent mixing region which is filled with turbulent structures that generate a large number of edges

$$\beta_{mix} = \frac{\frac{1}{H}\sum I(y)\Delta y}{max(I(y))}. \tag{1}$$

The behavior of the mixing parameter obtained after the analysis of the instantaneous images from the nozzle exit, plotted in Figure 9. Clearly, there is a rise to unity over the distance which has been qualitatively identified as the non-mixed length in the image (Figure 6). The oscillations on the trend are inherent due to the representation of intensity variation due to the presence of varied structures on limited spatial resolution of the image. But, on the whole the steady rise cannot be mistaken. By a series of comparisons between careful visual determination of the non-mixed length from a few of images of this case and that obtained algorithmically, the non-mixed length is defined as the location along the ejector where for the first time $\beta_{mix} = 0.95$ (this is important since the non-mixed length refers to the point until which the two flows appear distinct, any location thereafter is not considered). This definition is then applied to a set of 50 images for all the cases. Instantaneous images are analyzed separately and the average non-mixed length is computed from the mean of a set for every case. For the case under consideration, the non-mixed length is detected at about 260 mm which is 100 mm (5.0H, where H is the height of the mixing duct) from the exit of the nozzle.

2. Image processing of laser scattering images

A typical laser scattering snapshot during the flow at $P_{op} = 7.69$ bars and nozzle at Location A is shown in Figure 10. The seeded primary flow is made visible while the co-flowing secondary flow remains dark. As the tracers spread the intensity of light also spreads to the height of the ejector. The shock system of the primary flow is also visible in the picture. The non-mixed region is distinctly evident in the laser scattering image. A reduction in the intensity signal is observed among the images at different operating conditions close to the end of the mixing duct and the beginning of the diffuser. Dilution of the particle density due to transport and mixing, evaporation of droplets due to rising static pressures and temperatures; can be the reasons for the observation. Further, the

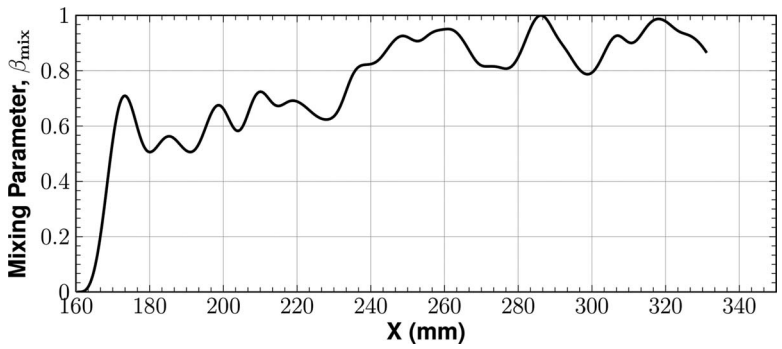

FIG. 9. β_{mix} vs X, obtained from the schlieren image along the ejector, nozzle exit at Location A, 160 mm.

secondary flow is not conditioned but directly sucked in from the ambient, hence the presence of humidity cannot be discounted. There is a possibility of this moisture producing fine water droplets by the product formation method.[21] Flow images have been taken without any seeding of acetone, where in scattering caused only by product formation are made apparent. The intensity of such scattering has been found to be negligible compared to the images taken with acetone seeding. The inferences on the non-mixed length are not affected by these factors since it lies much upstream (where the intensity of scattered light is higher and the primary flow and secondary flow are clearly distinguishable) and is the location where for the first time the primary and secondary flow loose their separate identity. There are stray reflections of the laser sheet from the walls of the ejector which are normalized using background subtraction and contrast adjustment techniques during the pre-processing stage of the image analysis of the laser scattering images.

The intensity profiles across the height of the ejector changes from a step profile close to the exit of the nozzle to a nearly uniform profile at the end of the non-mixed region. The progress of mixing is shown in the intensity profiles along the ejector plotted at different downstream distances from the nozzle exit in Figure 11.

The mixing parameter as defined in Eq. (1), can be applied to these intensity profiles also. The ratio of average to maximum intensity will be highest for a uniform profile and the least for a step profile. The mixing parameter for the laser scattering visualization is plotted in Figure 12 and the same criteria is used to identify the non-mixed length. The non-mixed length calculated from the laser scattering image is 94 mm (4.7 H) from the exit of the nozzle which agrees well with the one calculated from the schlieren image. Due to the limitation posed by the pulse rate of the laser, the number of images available per experimental condition is 20. Thus, both schlieren and laser scattering methods of flow visualization are used as complementary methods to visualize and quantitatively determine the non-mixed length of the flow through the supersonic ejector.

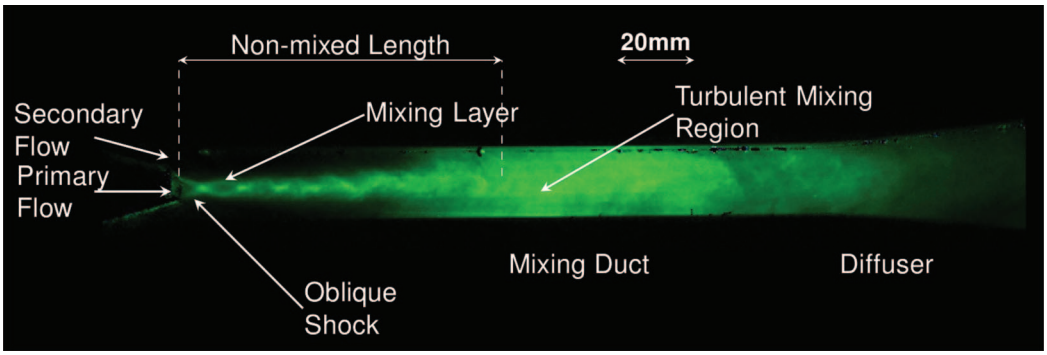

FIG. 10. A typical snapshot of the flow through an ejector by using the laser scattering flow visualization with the primary flow seeded with acetone at $P_{op} = 7.69$ bars, nozzle exit at Location A, 160 mm.

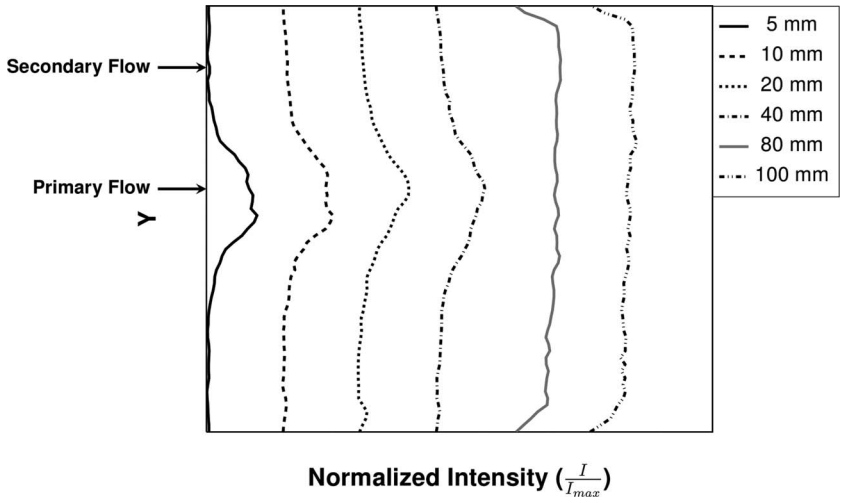

FIG. 11. Plot of the variation of intensity profiles at different downstream distances from the nozzle exit, $P_{op} = 7.69$ bars and nozzle at Location A, 160 mm.

Further, confirmative evidence to the above analysis is obtained by taking laser scattering images across transverse sections along the ejector (which have not been shown here for the sake of brevity[23]), which also show that by 100 mm from the nozzle exit the two flows indeed become indistinguishable. Clear schlieren images have been obtained for all the experimental conditions under consideration. Good laser scattering images could be obtained only at primary stagnation pressures of 7.69 bars and 9,69 bars. At 5.69 bars the quality of laser scattering images are poor, possibly due to insufficient condensation as the nozzle approaches highly overexpanded condition of operation. However, it has been established that the two techniques yield equivalent results hence inferences from either of the two visualization techniques hold good. To reemphasize, the non-mixed length is indicative of the mixing process within the ejector and does not mark the true end of mixing in the ejector. However, the trends on non-mixed length would throw light on the actual length of itself.

The digitized representation of the flow field with limited resolution, coupled with errors creeping in due to optical arrangements and processing algorithm contribute to a total uncertainty estimated to be about $\pm 7\%$ on the reported values of non-mixed length. The flow visualization experiments followed by the processing of images have been repeated at the same condition which show that the standard deviation ($<5\%$) over the ensemble averaged non-mixed length for three runs is within the limits of uncertainty.

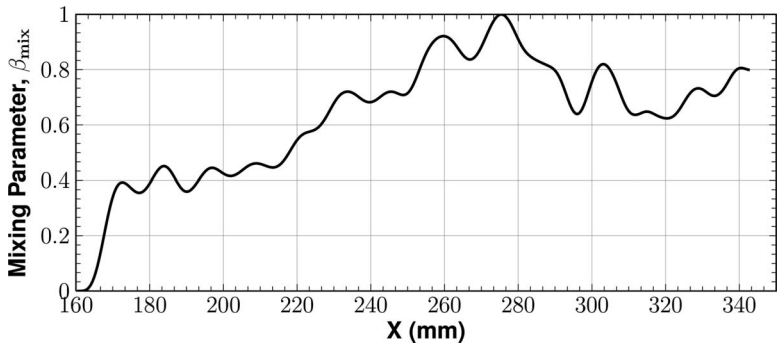

FIG. 12. β_{mix} vs X for the laser scattering image, nozzle exit at Location A, 160 mm.

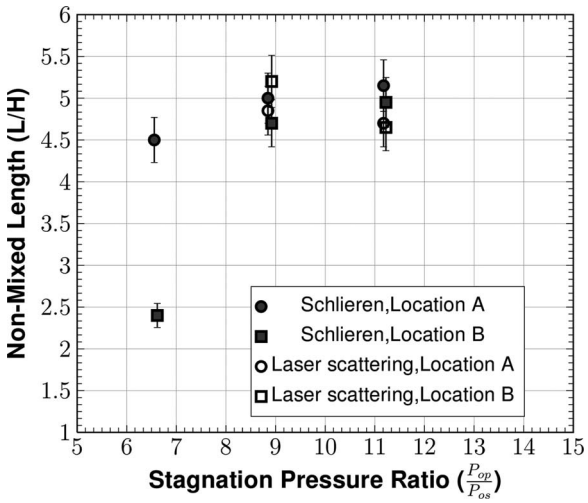

FIG. 13. The non-dimensionalized non-mixed length referenced from the nozzle exit vs the stagnation pressure ratio for two different locations of the nozzle in the ejector operating in the mixed regime.

V. RESULTS AND DISCUSSIONS

The elaboration of results and a comparative discussion at all experimental conditions are described in this section.

A. The non-mixed length

The non-mixed length from the exit of the nozzle (normalized by the mixing duct height H), computed from the flow images obtained from schlieren and laser scattering flow visualizations for all the six experimental conditions (Table I) is plotted against the corresponding stagnation pressure ratios in Figure 13. From the plot it is evident that for higher stagnation pressure ratios (7.69 bars and 9.69 bars), where data from both the flow visualization techniques are available, the results from schlieren and laser scattering images agree well with each other within the experimental uncertainty. This establishes schlieren and laser scattering methods of flow visualization as complementary techniques, corroborating the methods as well as the analysis of the images. The plot shows that for both the locations of the nozzle when the primary stagnation pressure is 7.69 bars and 9.69 bars, the non-mixed length is about 100 mm from the nozzle exit, (5.0 H). The non-mixed length decreases slightly with a decrease of stagnation pressure ratio ($L_{non-mix} = 4.5$ H, when $P_{op} = 5.69$ and nozzle at Location A). Considering the entire set, it can be seen that for most of the experimental conditions the non-mixed length lies in a narrow band of 4.5 H–5.2 H (90 mm–104 mm). However, clearly distinct from the rest there is a data point corresponding to experimental condition of primary stagnation pressure 5.69 bars and nozzle Location B where the non-mixed length is 49 mm (2.45 H), about 46.7% reduction from the case when the nozzle is at Location A. Unsteady shock-boundary layer interaction that occurs within the nozzle at this condition disturbs the shear layer causing enhancement of mixing and consequently a reduction in non-mixed length, which shall be elaborated in subsequent discussions. Thus, at appropriate conditions of operation significant enhancement of mixing and entrainment can be achieved and there is a good potential of exploiting this phenomenon to design short ejectors. These effects on the trends of the non-mixed length are traceable in the wall static pressure profiles which further confirm these observations and are discussed in detail in Sec. V B.

B. Nozzle exit at Location A, 160 mm

The wall static pressure plots for the three experimental conditions when the nozzle is located at Location A are plotted in Figure 14. Note that individual data points of a particular data set are joined by lines to indicate the trends with clarity. The schlieren images corresponding to these

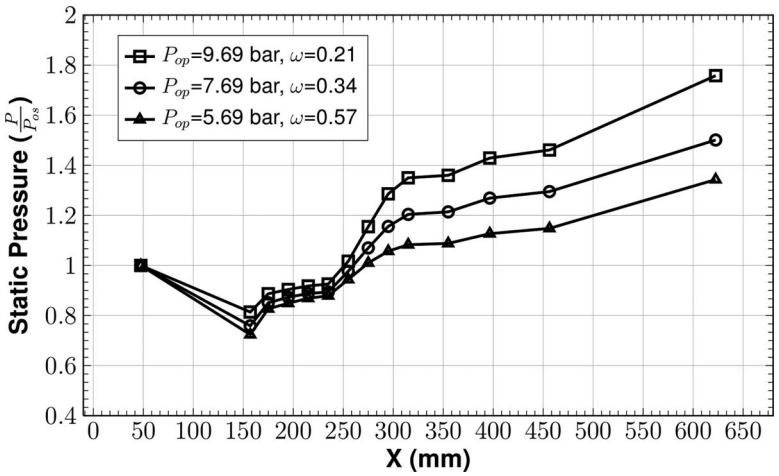

FIG. 14. Comparison of wall static pressure plots for the three experimental conditions [P_{op} = 9.69, 7.69, and 5.69 bars] when nozzle exit is at Location A, 160 mm.

conditions are given in Figure 15. The wall static pressure is non-dimensionalized by the pressure of the secondary flow at the secondary reservoir. From the secondary reservoir to the point of the nozzle exit a decrease of pressure can be observed due to the suction generated by the supersonic jet and the acceleration of the secondary flow. The mixing layer is thin for some distance downstream from the nozzle exit where the two co-flowing streams come in contact. The effects of shear stresses

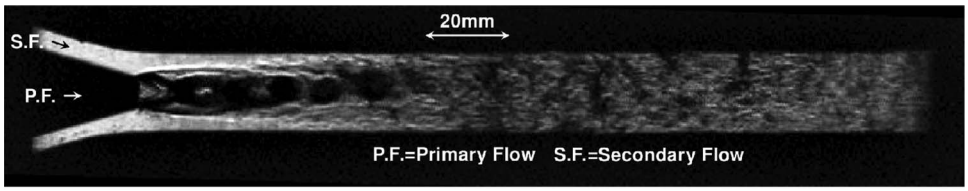

(a) Schlieren image P_{op}=9.69 bar, ω=0.21, Nozzle at Location A

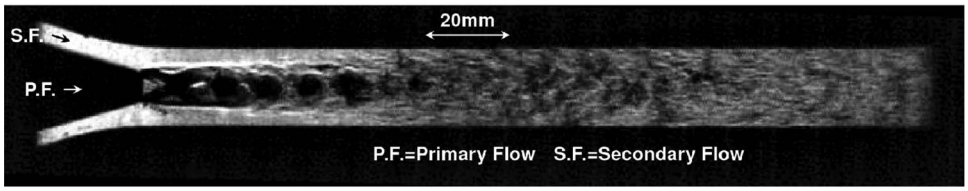

(b) Schlieren image P_{op}=7.69 bar, ω=0.34, Nozzle at Location A

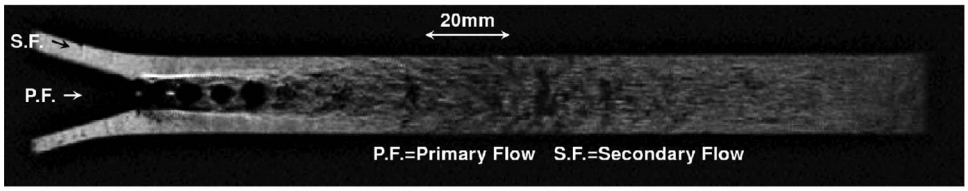

(c) Schlieren image P_{op}=5.69 bar, ω=0.57, Nozzle at Location A

FIG. 15. Comparison of instantaneous schlieren images for the three experimental conditions [P_{op} = (a) 9.69, (b) 7.69, and (c) 5.69 bars] when nozzle exit is at Location A, 160 mm.

are negligible in the bulk of the flow except at the mixing layers and wall boundary layers which are thin in this region. The primary flow contains shock cells, (5 shock cells are visible in the schlieren) which affect the shape of the jet boundary. The secondary flow is confined to flow within the passage between the jet boundary and the wall. The bulging of the jet boundary due to the expansion of the primary jet after exit from the nozzle is clearly visible in the schlieren image at the highest stagnation pressure ratio conditions, Figure 15(a), and its magnitude decreases with a reduction in primary stagnation pressure. The secondary flow continues to be accelerated by the convergence of the area between the wall and the jet boundary. At the end of the first shock cell (about 175 mm) the jet boundary is turned into itself due to the shock compression, providing a divergent area to the secondary flow. The ejector operates in the mixed regime, which is confirmed by the absence of any shocks in the secondary flow and the sensitivity of the ejector to backpressure changes. The average secondary flow Mach number at the entrance of the secondary flow into the mixing duct is calculated by considering uniform flow properties, the pressure measured close to the exit of the nozzle (at 157 mm), the secondary mass flow rate and using the isentropic gasdynamic relations (M_s lies between 0.3 [$P_{op} = 9.69$ bars] and 0.5 [$P_{op} = 5.69$ bars]). The critical secondary flow Mach number required such that choking occurs within the ejector passage can be estimated from Fabri's theory of choking (M_{sc} lies between 0.5 [$P_{op} = 9.69$ bars] and 0.9 [$P_{op} = 5.69$ bars]), and the comparison of these numbers definitively implies that the ejector operates in the mixed regime. Presenting a diverging passage to a subsonic flow decelerates it and increases the pressure. Further to this point the mixing layer can be seen thickening and occupies significant portion of the area. The secondary flow faces twin effects, the area decreases but greater mass of the secondary flow is entrained by the thickening mixing layer. The primary flow also experiences deceleration due to the effects of shear, mixing and shocks. This results in a near plateauing of the wall static pressure profile (the rate of rise in static pressure is very much small) between 175 mm and 235 mm. At 255 mm which is 95 mm downstream of the nozzle exit, the pressures sharply increase indicating larger mixing. This point lies in the turbulent mixing region at the end of the non-mixed region as estimated from the flow visualization images. The enhanced rates of interaction between the two flows and the greater deceleration of the primary flow is responsible for this rise in the slope of the pressure profile. Thus, the walls static pressures also corroborate the findings from the flow visualization. The point where the slope of the wall pressure profile undergoes a sudden increase can be taken as the end of the non-mixed region (non-mixed length). However, since the spatial distribution of the pressure sensors is limited (20 mm), only changes in non-mixed length of such magnitude are evident. For all the three conditions the non-mixed length lies at about 5.0 H (100 mm) from the nozzle exit as evidenced by the schlieren and the laser scattering visualizations, which is also reflected in the pressure profiles (255 mm is the end of non-mixed region for all three conditions). The pressure continues to rise in the constant area portion by the end of which the pressure profile turns to a second plateauing (315 mm–355 mm) and a nearly uniform subsonic flow can be seen in the schlieren image. The divergent diffuser provides the final pressure recovery (395 mm–625 mm) where another change in the slope of the wall pressure profile can be observed.

There are three distinct regions of the flow, which leave their footprint on the wall static pressure profiles. The initial non-mixed region consists of a drop in wall static pressure due to suction and then there is a plateauing at a higher pressure due to thickening mixing layer and decelerating primary flow. At the end of the non-mixed region the pressure profile jumps to higher pressures and by the end of the constant area duct the pressure profile reaches a second plateau. The final pressure recovery in the diffuser comes out as a further increase of pressure at a different slope of the profile. From the flow visualizations and the corresponding wall static pressure profiles the picture of the flow that has been explained is illustrated in Figure 16.

Comparing the three experimental conditions it can be seen that the static pressure at 157 mm is lowest when the stagnation pressure ratio is at its lowest. Simultaneously in the schlieren images the bulge of the jet boundary is the least for the same condition. A larger area is available for the secondary flow due to decreased expansion of the jet boundary. Hence the entrainment ratio and secondary flow rates are the highest at low stagnation pressure ratio. Correspondingly secondary flow Mach number is high at such conditions therefore wall static pressure is low. The behavior in non-mixed regime remains more or less similar for all the three curves. However, at the end of

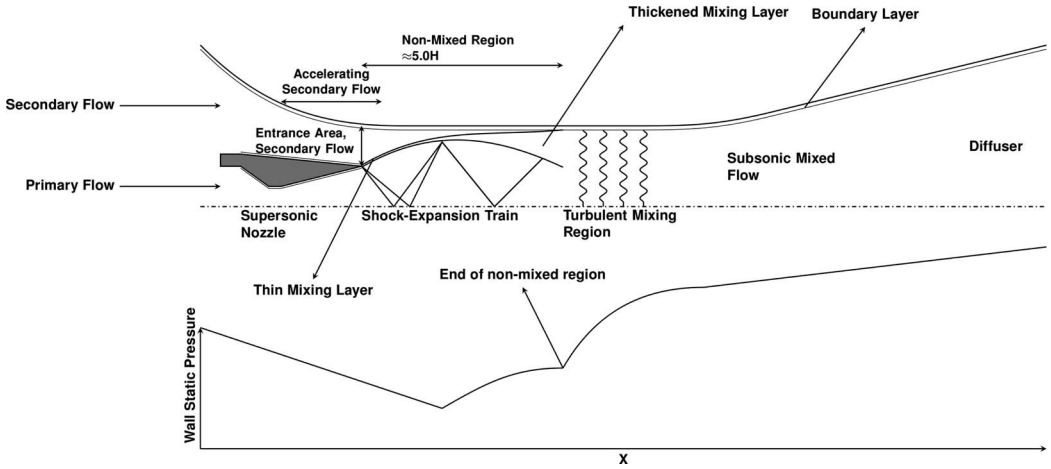

FIG. 16. An illustration of the flow within a supersonic regime inferred from flow visualizations and wall static pressure profile.

the non-mixed region the three curves separate with higher primary stagnation pressures leading to higher pressure recovery. Higher primary stagnation pressure implies higher capacity to do work on the secondary flow, besides higher primary mass flow rate accompanied by lower secondary flow rates leads to higher compression.

C. Nozzle exit at Location B, 145 mm

In this set of experiments the nozzle exit is pulled back upstream by 15 mm such that it lies in a converging duct. The area available to the secondary flow at the nozzle exit section increases by 71%. Consequent to this the secondary mass flow rate increases by 30%. A comparison of the wall static pressures between Location A and Location B for the same primary stagnation pressure of 7.69 bars is given in Figure 17 and the corresponding schlieren images in Figure 18.

From the schlieren images it is evident that overall flow features remain similar, and the upstream shift of the nozzle by 15 mm results in a corresponding shift in the flow features also. The shape of the pressure profile remains similar. The dramatic difference between the two is in the amount of suction at 157 mm which is far less when the nozzle is at Location B. The point of sudden upward

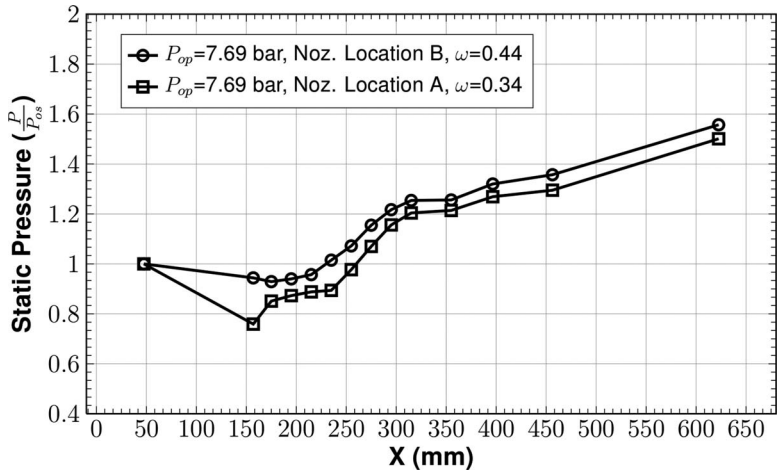

FIG. 17. Comparison of wall static pressure plots for the two corresponding experimental conditions [$P_{op} = 7.69$ bars] when nozzle is at Location A, 160 mm and Location B 145 mm.

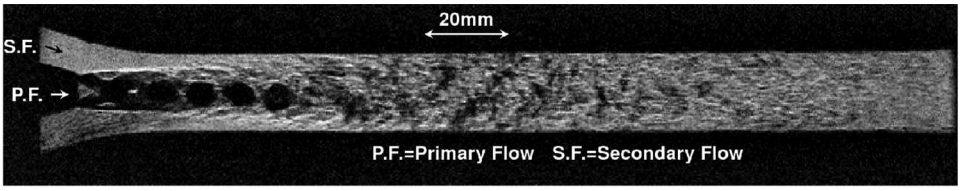

(a) Schlieren image P_{op}=7.69 bar, ω=0.44, Nozzle at Location B

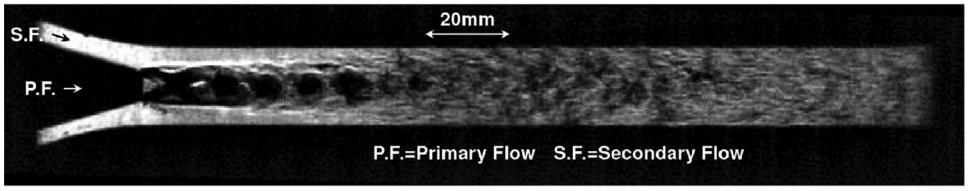

(b) Schlieren image P_{op}=7.69 bar, ω=0.34, Nozzle at Location A

FIG. 18. Comparison of instantaneous schlieren images for the two corresponding experimental conditions [$P_{op} = 7.69$ bars] when nozzle is at Location A, 160 mm and Location B, 145 mm.

rise that marks the end of non-mixed region is now at 235 mm (90 mm from the nozzle exit), which is an upstream shift due to the movement of the nozzle, implying that the non-mixed length remains almost the same as in Location A. This is also evident in the results of the analysis of the flow visualization images for $P_{op} = 9.69$ bars and 7.69 bars, $L_{non-mixed}$ which show that $L_{non-mixed}$ lies in the range 4.5 H–5.2 H, which is borne out by the static pressure profile also.

The entrained secondary flow is 30% more than the corresponding case when the nozzle is at Location A, however, the area available for the secondary flow is 71% higher which results in lower Mach numbers of the secondary flow ($M_s = 0.16$ [$P_{op} = 9.69$ bars] - 0.26 [$P_{op} = 5.69$ bars]) and hence higher pressures. Thus, the pressure at 157 mm is higher when the nozzle is located at Location B. Thereafter, the secondary flow faces convergence of area due to convergence of the wall and the expansion of the jet boundary with a simultaneous thickening of the mixing layer, hence the pressure reduces at 175 mm. This is counter to what has been observed in the pressure profile for nozzle Location A, where there is a drop at 155 mm and a rise at 175 mm. Further to this point, the flow happens in a constant area duct and the same plateauing effect before the end of the non-mixed region is observed.

The observation that increasing the area available to secondary flow increases the entrained flow rate begs an answer to what is the entrainment capacity of the ejector configuration. Simultaneously, there is a drop in suction pressure and increasing the area indefinitely will reach the limit of an open jet flow. That the relationship is not linear is clear from the numbers that though area increases by 71% the increase of flow rate is only 30%.

Figure 19 is a plot comparing the experimental and computational wall static pressure profiles at $P_{op} = 7.69$ bars and nozzle at Location B. The numerical agreement of the wall static pressures between CFD and experiment is within 20%. The limitation of the turbulence model in predicting the shear layer dynamics shows up in the difference between the static pressures, which have been observed by Bartosiewicz *et al.*[29] also. The Mach number contours for the same, displayed in Figure 20 shows that the flow features are qualitatively similar with what has been observed in the flow visualizations. Along the mixing duct the computational results show lower pressures than the experiments, as a consequence of which the primary flow remains supersonic for a greater length and shows as many as 7 shock cells. By the end of the mixing duct the flow is subsonic. The absence of sharp gradients in the schlieren at the end of the mixing duct also indicate a subsonic flow.

Higher pressures close to the nozzle exit when it is located at Location B, imply that the nozzle is facing higher levels of overexpansion (lower Nozzle Pressure Ratio - NPR). The operating NPR of the nozzle is calculated from the observed P_{op} and the pressure at 157 mm which is closest to

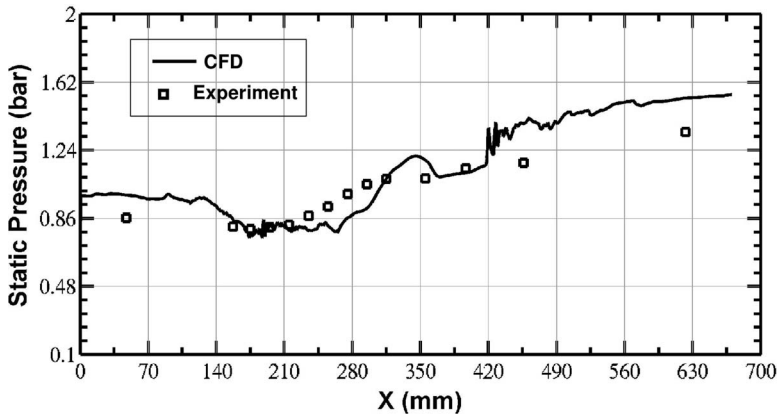

FIG. 19. Comparison between experimental and numerical wall static pressures, $P_{op} = 7.69$ bars and nozzle exit at Location B, 145 mm.

the nozzle exit. At the primary stagnation pressure of 5.69 bars and nozzle at Location B, the non-mixed length shows drastic reduction by 46.7% as compared to the same condition for the nozzle at Location A. The comparison of schlieren images for these two conditions are given in Figure 21 and the wall static pressures are in Figure 22.

From the schlieren image the drastic reduction in the non-mixed region when the nozzle is located at Location B is evident. In the wall static pressure profile, the sensor marking the end of non-mixed region is at 215 mm which is 70 mm from the nozzle exit. Thus, the reduction of non-mixed length is apparent in the flow visualization as well as in the wall static pressure profile. At this condition, the entrainment ratio is the highest among all the experimental conditions. This implies heightened entrainment and mixing. A closer look at the schlieren shows that the first shock cell that is clearly visible in the case of Location A is absent when the nozzle is at Location B. The inference is that this shock is located upstream within the nozzle, which is opaque. A shock within the nozzle duct interacts with the boundary layer, which further disturbs the mixing layer, thereby enhancing mixing and entrainment observed at this condition.

The enhancement of mixing from overexpanded nozzle has been observed in open jets previously,[30] where the cause of the effect has been attributed to shock-boundary layer interactions. To ascertain that the nozzle is indeed severely overexpanded to cause this effect, the semi-empirical formula developed by Arens and Spiegler[31] (Eq. (2)) is used from which the nozzle NPR $\left(\frac{P_{op}}{P_{noz-exit}}\right)$ for incipient shock-boundary layer interaction and the location of the separation in the nozzle duct

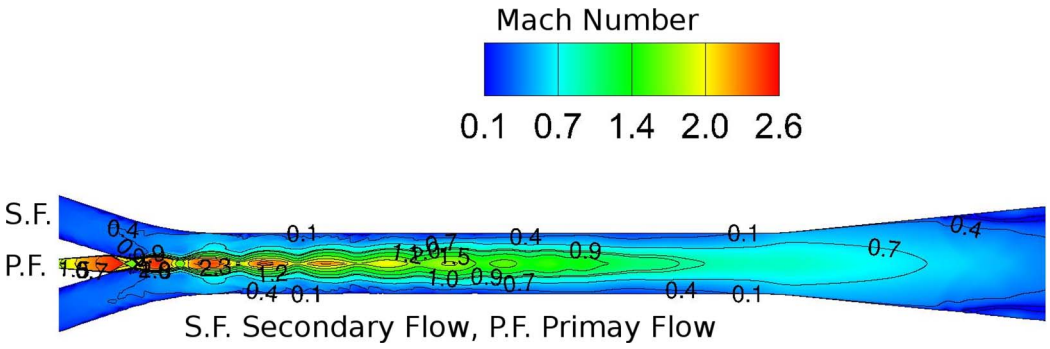

FIG. 20. Mach number contours at $P_{op} = 7.69$ bars and nozzle exit at Location B, 145 mm.

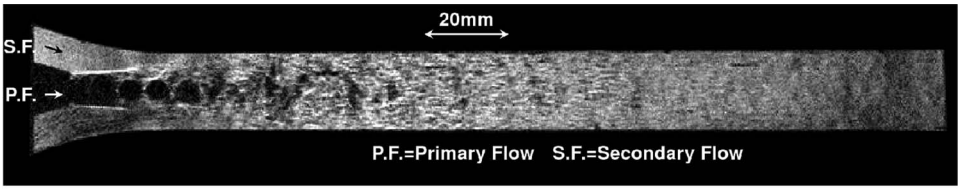

(a) Schlieren image P_{op}=5.69 bar, ω=0.69, Nozzle at Location B

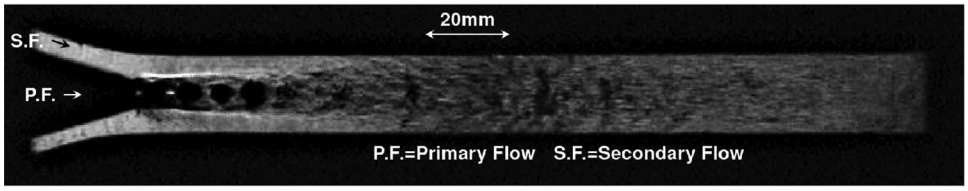

(b) Schlieren image P_{op}=5.69 bar, ω=0.57, Nozzle at Location A

FIG. 21. Comparison of instantaneous schlieren images for the two corresponding experimental conditions [$P_{op} = 5.69$ bars] when nozzle is at Location A, 160 mm and Location B, 145 mm.

can be calculated as

$$\frac{P_{sep}}{P_{noz-exit}} = \frac{\frac{P_{op}}{P_{noz-exit}}}{\left[\frac{(P_{op}/P_{noz-exit})-(u_s{}^*/u_s)^2}{1-(u_s{}^*/u_s)^2}\right]^{\frac{\gamma}{\gamma-1}}}. \tag{2}$$

Here P_{sep} and M_{sep} are the static pressure and Mach number at the point of separation. The theory stipulates that at the point of separation a reference velocity in the boundary layer $u_s{}^*/u_s$ goes to zero. Considering experimental data from various sources, the value of $u_s{}^*/u_s = 0.6$ has been determined for nozzles, within experimental scatter. The NPR of the nozzle is $P_{op}/P_{157\,\mathrm{mm}}$, hence P_{op}/P_{sep} can be calculated. Assuming the flow is isentropic until the separation point M_{sep} can be calculated. Then the location of separation point is computed from the quasi-1D isentropic relations. Calculations using this method give a NPR = 7.8, below which separation of boundary layer due to shock interaction occurs in the nozzle. The NPR of the nozzle at Location B for $P_{op} = 5.69$ bars is 7.09 (it is 9.06 when the nozzle is at Location A), thus shock separating the boundary layer inside the nozzle can be expected. The oblique shock lies within the nozzle, calculations show that it is

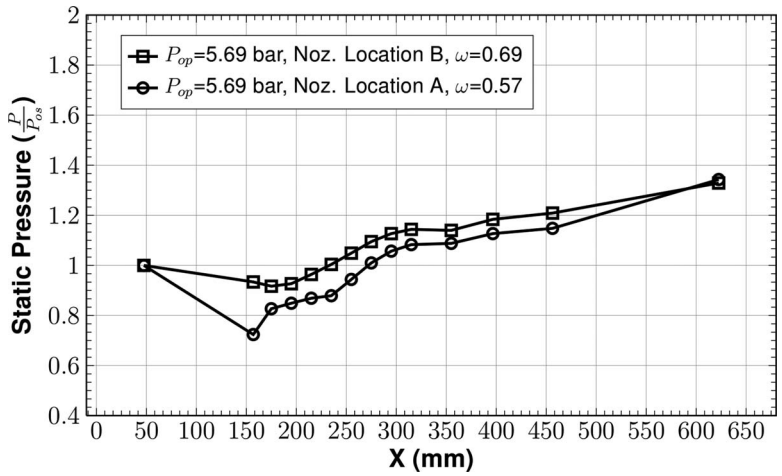

FIG. 22. Comparison of wall static pressure profile plots for the two corresponding experimental conditions [$P_{op} = 5.69$ bars] when nozzle is at Location A, 160 mm and Location B, 145 mm.

about 3 mm upstream of nozzle exit. Such flows are unsteady in nature, the location of shock as well as the point of separation keeps moving back and forth, and have a destabilizing effect on the mixing layer,[30] which enhances the mixing rate of the mixing layer.

The supersonic nozzle is covered by opaque wall on the sides which prevent observation by flow visualization. Supportive evidence is sought form numerical results, which have been shown to be compliant with the experimental results.

A comparison of the close up vector plots between the case of nozzle located at Locations A and B at $P_{op} = 5.69$ bars (Figure 23) shows without doubt that the nozzle flow is separated in the case when the nozzle is at Location B and there is no separation in the other. This confirms that the drastic reduction of non-mixed length and enhanced mixing is indeed due to shock-boundary layer interaction within the nozzle. The essence of the flow dynamics at this peculiar operating condition is illustrated in Figure 24. Thus operating the supersonic ejector at such conditions that the nozzle is overexpanded to an extent that the mixing enhancement can occur seems to be beneficial to the performance of the ejector. However, more studies need to be conducted on the consequences to structures due to the unsteady loads offered by such a flow and the efficiency of this mechanism as compared other methods of mixing enhancement in supersonic flows[32] before adopting the method.

This discussion of results in a two dimensional rectangular ejector has focused on the statistically steady behavior of the flow features in the ejector. The existence of a tangible statistically steady mean flow with a small fluctuation of parameters ($<2\%$ about the mean) justifies this detailed discussion. Time-resolved schlieren images also show that there are oscillations of the shock cells about a mean location, unsteady vortices in the mixing layer, and a range of unsteady structures in the turbulent mixing region which can be seen in the sequence of schlieren images (time interval of 5 ms between consecutive images) in Figure 25. Overall, a typical steady picture described before holds good. Section V D explores the unsteady fluctuations using the schlieren images and the recorded pressure signal.

D. The unsteady flow field

From a series of schlieren images a repetitive forward-backward motion of the shock cells is evident. To get a better understanding of this shock motion, intensity profile is mapped at every image for the central line of the ejector that passes through the shock cells. These intensity profiles are stacked one after the other resulting in a time trace of the intensity at a point along the line. Note that these images are taken during the test time of ejector operation, and for time based analysis of the images 200 images are considered for an experimental run. The resulting composite image is shown in Figure 26. There are five shock cells visible in the image taken at $P_{op} = 9.69$ bars, nozzle at Location A. In the trace of shock motion five distinct bars can be observed, each showing an intensity peak moving back and forth. Clearly, this is a case of shock motion about a mean location. The turbulent regions beyond the core of the supersonic jet are filled with random variations of intensity denoting the end of a separate primary core flow. Intensity scanning is done at the five locations corresponding to each bar of shock cell. The instantaneous location of the shock, seen as an intensity peak in the vicinity of the mean location, can be computed. Figure 27 shows the motion of shock cells 1 and 3 in physical units, showing that the maximum peak to peak amplitude is about 5 mm and that the amplitude of shock motion is lesser close to the nozzle exit and increases downstream. This is significant considering that the exit height of the supersonic nozzle is 6 mm, the amplitudes of shock oscillations are also of the same order. A significant point to notice in the plot and the composite image is that the trace of each shock cell follows the other, i.e., there is a strong correlation between shock motions of each shock cell and they move together. However, the amplitude of individual shock cells is not the same, implying a change of shock cell size. This is confirmed by calculating the statistical correlation coefficient (which is a ratio of the covariance of two data sets to the product of their standard deviations[33]) between two consecutive traces. The correlation coefficient of the instantaneous shock cell locations for the case under consideration between shock cell 1 and 2; shock cell 2 and 3; shock cell 3 and 4; shock cell 4 and 5 are 0.63, 0.92, 0.89, and 0.81, respectively. These values indicate a concerted motion of the shocks. The peak to peak amplitude in the order of shock cell from the exit of the

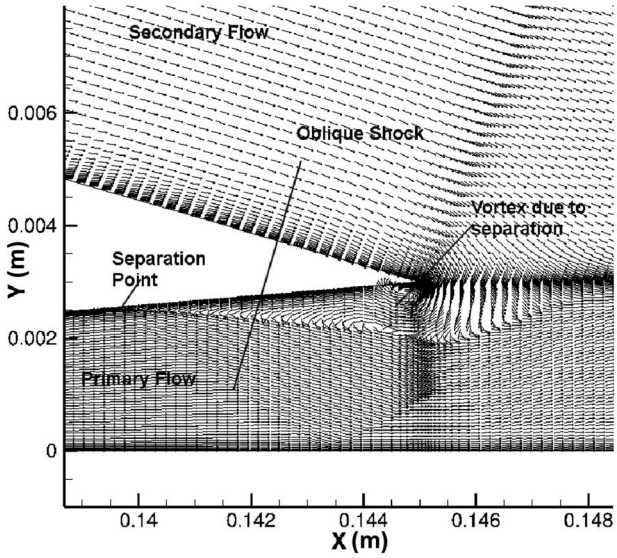

(a) Close up vector plot P_{op}=5.69 bar, Nozzle at Location B

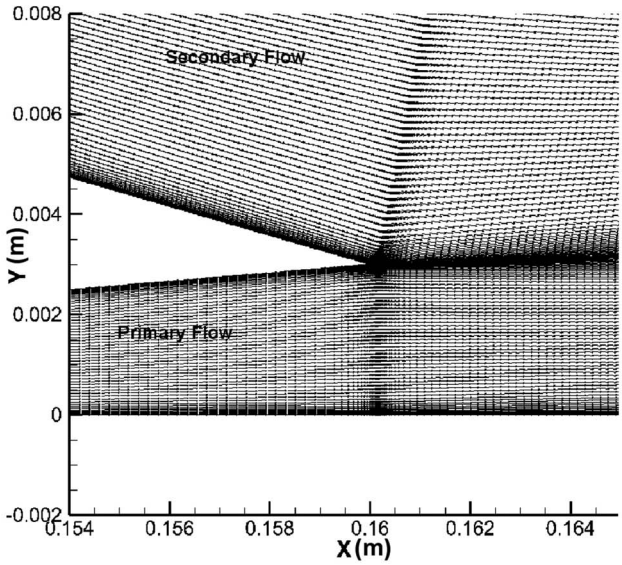

(b) Close up vector plot P_{op}=5.69 bar, Nozzle at Location A

FIG. 23. Comparison of close up vector plots obtained from CFD computations for the two corresponding experimental conditions [P_{op} = 5.69 bars] when nozzle is at Location A, 160 mm and Location B, 145 mm.

nozzle is (1.1 mm, 2.8 mm, 4.6 mm, 3.9 mm, 3.7 mm), showing that there is a change of the shock cell shape. A combination of up-down and front-back motions of the shock cells and the jet boundary is also observed in the schlieren images. Another important point is that maximum amplitudes of the motion are found along the centerline of the supersonic jet while the anchor of the shock cell at the jet boundary seems to move relatively less. From repeated schlieren experiments a typical average power spectrum of the time trace of fluctuations of the third shock cell is shown in Figure 28. Discrete frequency peaks are seen – 50 Hz, 75 Hz. The wall static pressure should record

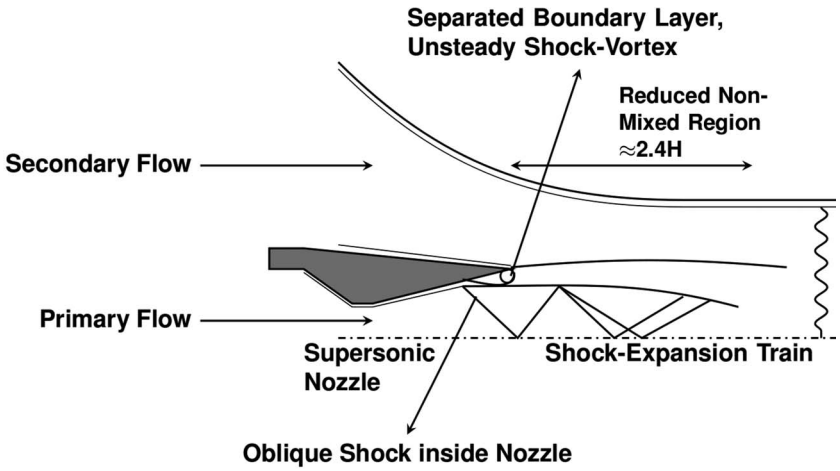

FIG. 24. A schematic of the near field flow at the nozzle exit section when the ejector operates at such conditions that the nozzle is severely overexpanded and non-mixed length is reduced.

some indication of these fluctuations in the shock location. The average power spectrum of the signal in Kulite sensor at 215 mm which is closest to the location of the shock cell, shown in Figure 29, also show discrete peaks among which the dominant one is at 60 Hz.

The power spectrum obtained using the Kulite pressure signal is better resolved in frequency domain because of the sampling rate being 20 kHz and data being available for a second. The sampling rate of schlieren images is 2 kHz and the memory requirements limit the image storage to just 0.1 s, hence the frequency resolution is rather coarse. Despite this difference in sampling rate the spectra agree well qualitatively. Discrete peaks of significant amplitude are found within 100 Hz. The analysis of schlieren images to yield data on the shock motion finds support in the wall static pressure measurements also.

The mixing layer grows between the primary flow and secondary flow in a space limited by the walls of the duct. A large number of unsteady vortical structures can be observed in the mixing layer especially when it becomes thick. The edge of this layer is thus jagged, and as the structures

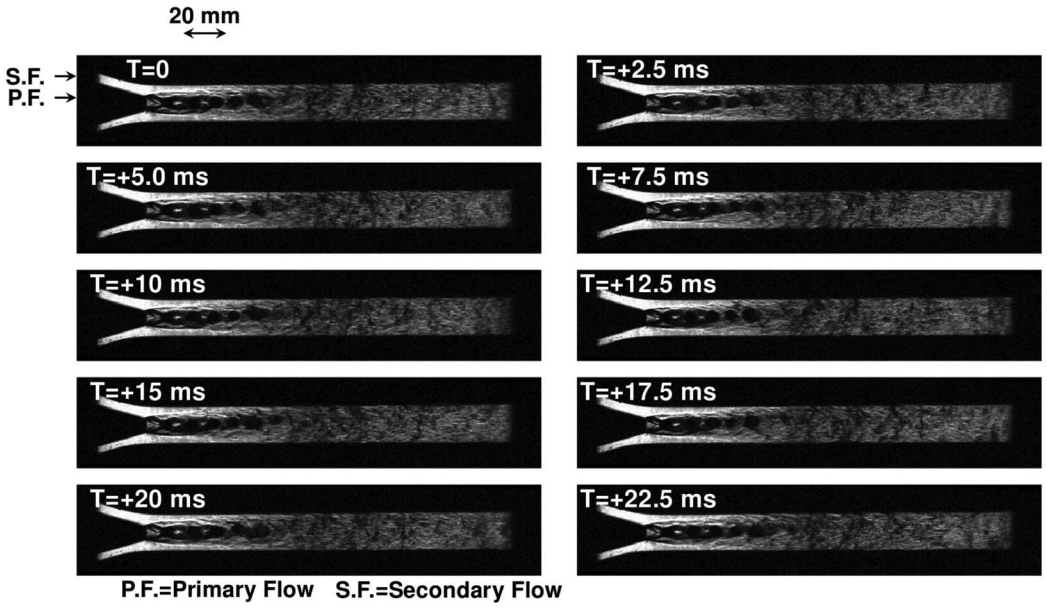

FIG. 25. A sequence of schlieren snapshots at $P_{op} = 9.69$ bars, nozzle exit at Location A, 160 mm.

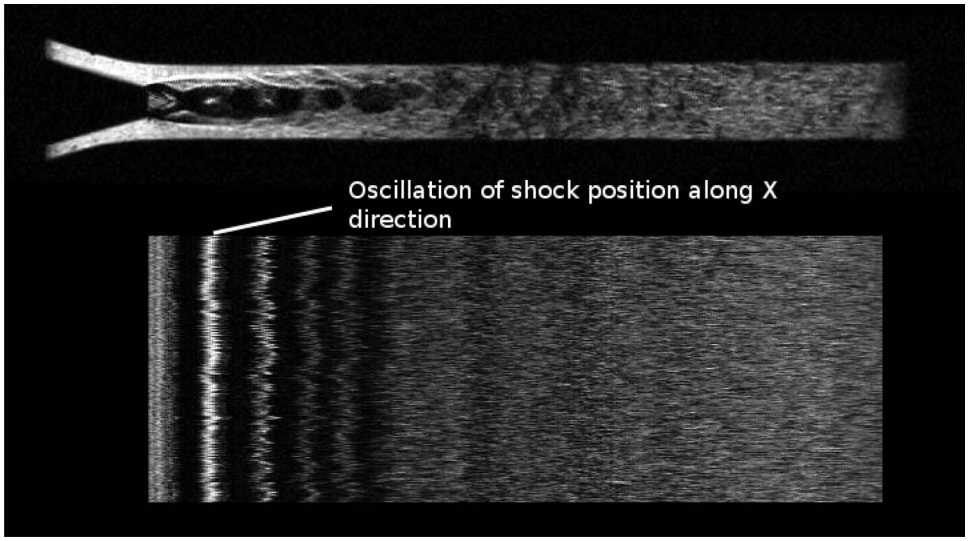

FIG. 26. A composite image showing the trace of shock cell motion at the central line of the ejector.

form, grow, and interact with the two fluids they introduce fluctuations to the flow quantities like velocity and pressure. The presence of wall emphasizes such disturbances since unlike open domain flows the effects can reflect off the wall back into the duct. This results in the response of the shock system as it adjusts to fluctuating pressure conditions. The flow topology also introduces a varying mean static pressure upon the jet boundary, which has the effect of enhancing the amplitudes of shock motion when moving downstream along the ejector [small amplitudes and variation of the shock shape close to the exit of the nozzle are amplified downstream]. There have been studies on shock oscillations in a supersonic jet exiting to the ambient that cause screech tones, among which a detailed study by Panda[34] is significant in this regard. The remarkable observation that amplitudes of oscillations are more at the centerline than at the jet boundary has also been made in open supersonic jets. Though interaction of shocks with turbulence and aeroacoustic perturbations of the jet mixing layer are the source of these oscillations, maximum amplitudes are encountered at the center of the jet. The situation gets accentuated in the presence of a confined duct with a co-flow. The possibility of resonant standing modes of the duct affecting these motions cannot be discounted. Through this study a clear observation and quantification of shock oscillations in an ejector has been made.

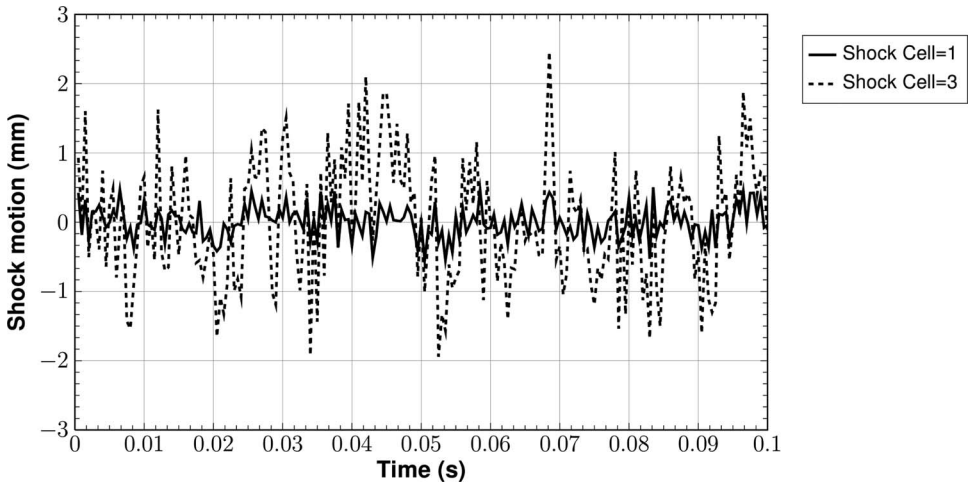

FIG. 27. The plot of fluctuation of shock location from the mean determined from time resolved schlieren images.

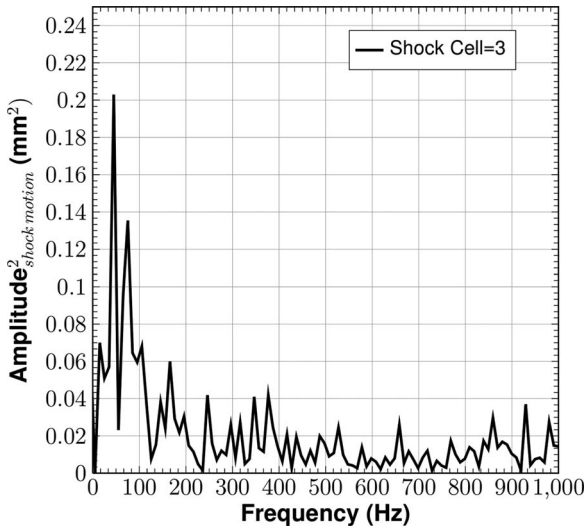

FIG. 28. Average power spectrum of the shock motion observed in time resolved schlieren images.

Thus the flow picture that emerges from the analysis of time resolved schlieren images and the wall static pressure signals is shown in Figure 30. A fluctuation of the shock location is observed about a mean location at each shock cell location. Analysis of these peaks shows that all shock cells move in the same direction at any given time, either forward or backward. The amplitude of motion is not same between the shock cells implying a change of shape of the shock cell. The minimum peak to peak amplitude is always at the first shock cell, and the maximum amplitude occurs at the third or fourth shock cell. This behavior is observed in all the experiments conducted. Analysis at the other operating conditions have shown that the general picture of shock motions (maximum amplitudes are about the height of the duct and the dominant frequency is in the vicinity of 100 Hz) hold with minor variations on the magnitude. The study being limited in its scope to address the issue of unsteadiness in shock motion per se, it is difficult to ascertain clear trends in this regard and a future detailed study should throw more light. Given the observations of shock oscillations in the ejector and the need for improvement of mixing in such devices, a proposition is advanced—that there are optimal designs of the mixing duct with aeroacoustic characteristics such that these oscillations can be put to beneficial use for mixing enhancement by the mutual interactions of unsteady shocks and vortices.

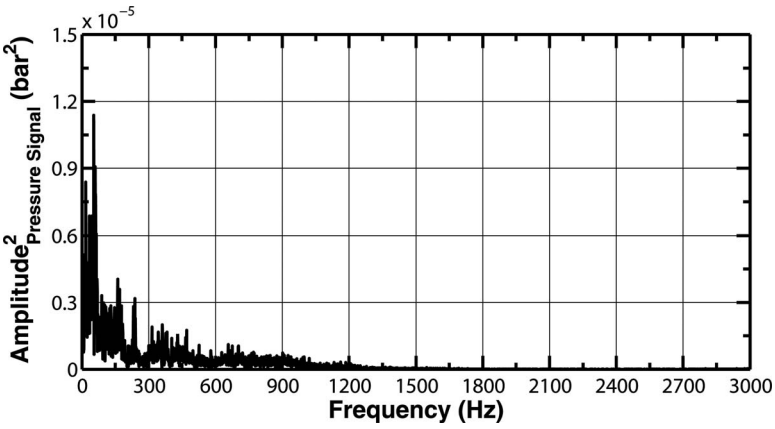

FIG. 29. Average power spectrum of pressure signal from the Kulite sensor at 215 mm, during the test time.

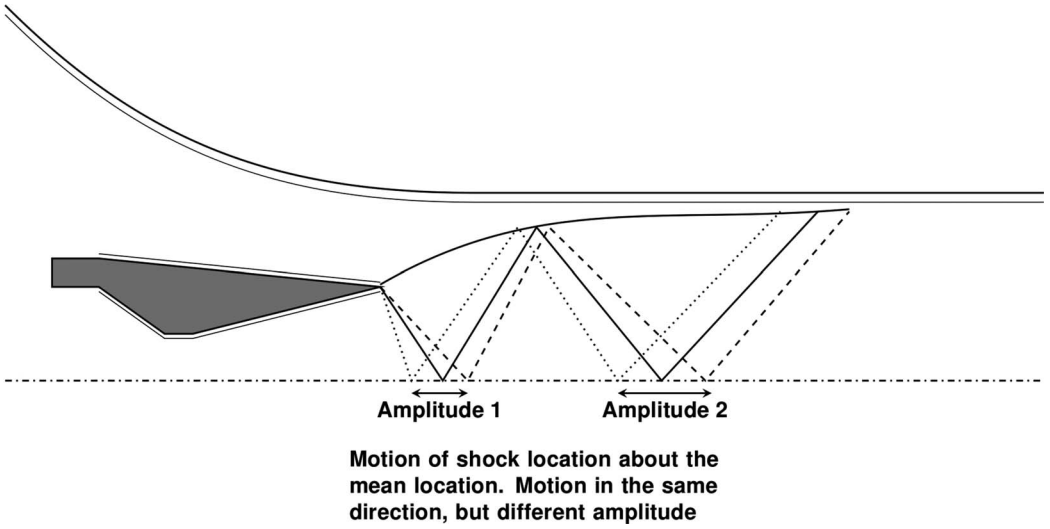

FIG. 30. A schematic illustration of the unsteady shock motion observed in the ejector.

VI. CONCLUSIONS

Experimental investigations on a two dimensional rectangular ejector have been carried out with an aim to provide a consistent understanding of the flow thorough a supersonic ejector at various operating conditions, using wall static pressure measurements and flow visualization techniques—the time resolved schlieren and the laser scattering technique. The rectangular supersonic ejector has an area ratio of 3.33, with a primary supersonic nozzle of designed Mach number, 2.48. Experiments are carried out on the ejector for a range of stagnation pressure ratios from 6.61 to 12.55, and entrainment ratios ranging between 0.15 and 0.69. For all the conditions, the ejector has been found to be operating in the mixed regime, where the entrainment ratio is strongly influenced by the backpressure. The non-mixed length, which is directly related to the mixing in the ejector, is a crucial parameter of interest in these experiments. Image processing algorithms developed for both the visualization techniques are used to determine them from a series of flow images at the particular experimental condition. Consistency has been found between results obtained from schlieren as well as laser scattering images establishing them as complementary tools and corroborating the image analysis procedure. The non-mixed length has been found to lie in a narrow band of 4.5 H–5.2 H from the nozzle exit and has seen little influence despite varying the operating parameters of the ejector flow. Further evidence pointing to the validity of the non-mixed length determination is found in the behavior of the mean wall static pressure profile along the ejector. The wall static pressure profile shows a suction region close to the exit of the nozzle where the supersonic flow accelerates the secondary flow and the mixing layer is thin. Further, as the mixing layer grows thick the pressure profile undergoes a plateauing at a higher pressure. At the end of non-mixed region as seen in the flow visualization images, the wall static pressure takes a turn to rapid pressure recovery in a constant area duct signifying rapid exchange of momentum between the two flows and a loss of their separate identities. Thus, through the set of experiments using multiple tools a consistent flow picture is described, where one to one relation between the flow visualizations and the corresponding wall static pressure measurement is brought out. Only a separation within the nozzle due to shock-boundary layer interaction has produced a drastic change in the mixing length. This might be because only a nozzle of Mach number 2.48 has been tested in these set of experiments. Upon separation of boundary layer, the resulting flow resembles a supersonic jet but of a different nozzle profile. The effect of primary Mach number on mixing within the ejector needs further investigations. Pulling the nozzle location 15 mm upstream into the convergent section of the ejector has the effect of increasing the area available for secondary flow entrainment and hence results in an increase of secondary mass flow rate and consequently the entrainment ratio (30% increase in entrainment ratio is observed).

The increased cross sectional area reduces the acceleration of secondary flow, hence, there is an increase in wall static pressures in the initial region close to the exit of the nozzle. Particularly, this increase of static pressure causes the first shock cell to move within the supersonic nozzle at significantly low stagnation pressure ratios, which causes a boundary layer separation in the nozzle. Such a flow has a marked reduction of non-mixed length by about 46.7%.

The unsteadiness of the flow is analyzed from time resolved schlieren images and confirmed through analysis of the relevant pressure signal. The analysis shows that there is backward-forward motion of the shock cells (maximum amplitude at centerline is about 5 mm which is about the order of the height of the nozzle), which happens together for all the shock cells, but at different amplitudes. This implies that shock cells are deforming to different shapes along with a motion in a particular direction. The power spectrum obtained from schlieren images and from a pressure sensor closest to the oscillating shock are similar accrediting the inferences from the unsteady image data.

Thus, in essence a consistent understanding of flow in the mixed regime through a supersonic ejector has been achieved by utilizing different flow analysis tools. Further studies are being carried out to address the dependence of the mixing characteristics on the primary nozzle geometry and on shock oscillations in such complex flow scenario.

ACKNOWLEDGMENTS

The authors would like to acknowledge the financial grants from Tata Motors and Defense Research and Development Organization (DRDO), India, towards the study. The authors are thankful to the members of the laboratory for their help during the study. The authors are grateful to the constructive review and comments of the reviewers which have helped improve the article.

[1] R. B. Fancher, "Low-area ratio, thrust-augmenting ejectors," J. Aircr. **9**(3), 243–247 (1972).
[2] M. Alperin and J.-J. Wu, "Thrust augmenting ejectors Part I," AIAA J. **21**(10), 1428–1436 (1983).
[3] M. Alperin and J.-J. Wu, "Thrust augmenting ejectors Part II," AIAA J. **21**(12), 1698–1706 (1983).
[4] Chen Jian, Wu Jiping, Wang Zhenguo, and Luo Wenlei, "The effect of secondary flows on the starting pressure for a second-throat supersonic ejector," J. Therm. Sci. **20**(6), 503–509 (2011).
[5] Zou Jian-Jun, Zhou Jin, Lu Hui-Giang, and Hu Yong, "Experimental investigation on starting process of supersonic single-stage air ejector," J. Therm. Sci. **21**(4), 348–353 (2012).
[6] K. Annamalai, T. N. V. Satyanarayana, V. Sriramulu, and K. A. Bhaskaran, "Development of design methods for short cylindrical supersonic exhaust diffuser," Exp. Fluids **29**, 305–308 (2000).
[7] B. J. Huang, C. B. Jiang, and F. L. Hu, "Ejector performance characteristics and design analysis of jet refrigeration system," Trans. ASME J. Fluids Eng. **107**, 792–802 (1985).
[8] K. Chunnanond and S. Aphornratana, "Ejectors: Applications in refrigeration technology," Renewable Sustainable Energy Rev. **8**, 129–155 (2004).
[9] J. C. Dutton, C. D. Mikkelsen, and A. L. Addy, "A theoretical and experimental investigation of the constant area supersonic-supersonic ejector," AIAA J. **20**(10), 1392–1400 (1982).
[10] M. L. Ferrari, D. Bernardi, and A. F. Massardo, "Design and testing of ejectors for high temperature fuel cell hybrid systems," Trans. ASME J. Fuel Cell Sci. Technol. **3**, 284–291 (2006).
[11] J. H. Keenan, E. P. Neumann, and F. Lustwerk, "An investigation of ejector design by analysis and experiment," Trans. ASME J. Appl. Mech. **72**, 299–309 (1950).
[12] A. L. Addy, J. C. Dutton, and C. D. Mikkelensen, "Supersonic ejector-diffuser theory and experiment" (Report, University of Illinois, Urbana, 1981).
[13] P. Desevaux, "A method for visualizing the mixing zone between two co-axial flows in an ejector," Opt. Lasers Eng. **35**, 317–323 (2001).
[14] J. Fabri and J. Paulon, "Theory and experiment on supersonic air-to-air ejectors," NACA Technical Memorandum 1410, 1958.
[15] K. R. Hedges and P. G. Hill, "Compressible flow ejector Part 2. Flow field measurements and analysis," J. Fluids Eng. **96**, 282–288 (1974).
[16] K. Chunnanond and S. Aphornratana, "An experimental investigation of a steam ejector refrigerator: the analysis of the pressure profile along the ejector," J. Appl. Therm. Eng. **8**, 129–155 (2003).
[17] V. Dvorak and P. Safarik, "Supersonic flow structure in the entrance part of a mixing chamber of 2D model ejector," J. Therm. Sci. **12**(4), 344–349 (2003).
[18] V. Dvorak and P. Safarik, "Transonic instability in the entrance part of a mixing chamber of high-speed ejector," J. Therm. Sci. **14**(3), 260–271 (2005).
[19] K. B. M. Q. Zaman, "Spreading characteristics of compressible jets from nozzles of various geometries," J. Fluid Mech. **383**, 197–228 (1999).
[20] D. Papamoschou and A. Roshko, "The compressible turbulent shear layer: An experimental study," J. Fluid Mech. **197**, 453–477 (1988).

[21] N. T. Clemens and M. G. Mungal, "Large-scale structure and entrainment in the supersonic mixing layer," J. Fluid Mech. **284**, 171–216 (1995).
[22] M. V. Srisha Rao and G. Jagadeesh, "Vector evaluated particle swarm optimization (VEPSO) of supersonic ejector for hydrogen fuel cells," J. Fuel Cell Sci. Technol. **7**(4), 041014-1–041014-7 (2010).
[23] M. V. Srisha Rao, "Experimental investigations on supersonic ejectors," Ph.D. thesis (Indian Institute of Science, 2013).
[24] M. V. Srisha Rao and G. Jagadeesh, "Visualization and image processing of compressible flow in a supersonic gaseous ejector," J. Indian Inst. Sci. **93**(1), 57–66 (2013).
[25] G. S. Settles, *Schlieren and Shadowgraph Techniques* (Springer, 2001).
[26] P. D. Kovesi, "MATLAB and Octave Functions for Computer Vision and Image Processing," Centre for Exploration Targeting, School of Earth and Environment, The University of Western Australia. Available from ⟨http://www.csse.uwa.edu.au/∼pk/research/matlabfns/⟩ (2000).
[27] I. Mcgregor, "The vapor-screen method of flow visualization," J. Fluid Mech. **11**, 481–511 (1961).
[28] N. T. Clemens and M. G. Mungal, "A planar Mie scattering technique for visualizing supersonic mixing flows," Exp. Fluids **11**, 175–185 (1991).
[29] Y. Bartosiewicz, Z. Aidoun, P. Desevaux, and Y. Mercadier, "Numerical and experimental investigations on supersonic ejectors," Int. J. Heat Fluid Flow **26**, 56–70 (2005).
[30] D. Papamoschou and A. D. Johnson, "Mixing enhancement from severely overexpanded nozzles," Int. J. Aerosp. Innovations **2**(4), 235–252 (2010).
[31] M. Arens and E. Spiegler, "Shock-induced boundary layer separation in overexpanded conical exhaust nozzles," AIAA J. **1**(3), 578–581 (1963).
[32] E. J. Gutmark, K. C. Schadow, and K. H. Yu, "Mixing enhancement in supersonic free shear flows," Annu. Rev. Fluid Mech. **27**, 375–417 (1995).
[33] J. P. Marques, *Applied Statistics Using SPSS, STATISTICA, MATLAB and R* (Springer, 2007).
[34] J. Panda, "Shock oscillation in underexpanded screeching jets," J. Fluid Mech. **363**, 173–198 (1998).